DES 2017-0238
Fermilab PUB-17-349-AE

MNRAS **000**, 1–11 (2015) Preprint 19 September 2017 Compiled using MNRAS LaTeX style file v3.0

Deep SOAR follow-up photometry of two Milky Way outer-halo companions discovered with Dark Energy Survey

E. Luque,[1,2]⋆ B. Santiago,[1,2] A. Pieres,[1,2] J. L. Marshall,[3] A. B. Pace,[3] R. Kron,[4,5] A. Drlica-Wagner,[4] A. Queiroz,[1,2] E. Balbinot,[6] M. dal Ponte,[1,2] A. Fausti Neto,[2] L. N. da Costa,[2,7] M. A. G. Maia,[2,7] A. R. Walker,[8] F. B. Abdalla,[9,10] S. Allam,[4] J. Annis,[4] K. Bechtol,[11] A. Benoit-Lévy,[9,12,13] E. Bertin,[12,13] D. Brooks,[9] A. Carnero Rosell,[2,7] M. Carrasco Kind,[14,15] J. Carretero,[16] M. Crocce,[17] C. Davis,[18] P. Doel,[9] T. F. Eifler,[19,20] B. Flaugher,[4] J. García-Bellido,[21] D. W. Gerdes,[22,23] D. Gruen,[18,24] R. A. Gruendl,[14,15] G. Gutierrez,[4] K. Honscheid,[25,26] D. J. James,[27] K. Kuehn,[28] N. Kuropatkin,[4] R. Miquel,[16,29] R. C. Nichol,[30] A. A. Plazas,[20] E. Sanchez,[31] V. Scarpine,[4] R. Schindler,[24] I. Sevilla-Noarbe,[31] M. Smith,[32] M. Soares-Santos,[4] F. Sobreira,[2,33] E. Suchyta,[34] G. Tarle[23] and D. Thomas[30]

Affiliations are listed at the end of the paper

Released 19 September 2017

ABSTRACT

We report the discovery of a new star cluster, DES 3, in the constellation of Indus, and deeper observations of the previously identified satellite DES J0222.7−5217 (Eridanus III). DES 3 was detected as a stellar overdensity in first-year Dark Energy Survey data, and confirmed with deeper photometry from the 4.1 metre Southern Astrophysical Research (SOAR) telescope. The new system was detected with a relatively high significance and appears in the DES images as a compact concentration of faint blue point sources. We determine that DES 3 is located at a heliocentric distance of ~ 76 kpc and it is dominated by an old ($\simeq 9.8$ Gyr) and metal-poor ($[\mathrm{Fe/H}] \simeq -1.88$) population. While the age and metallicity values of DES 3 are similar to globular clusters, its half-light radius ($r_\mathrm{h} \sim 6.5$ pc) and luminosity ($M_V \sim -1.9$) are more indicative of faint star clusters. Based on the apparent angular size, DES 3, with a value of $r_\mathrm{h} \sim 0\farcm3$, is among the smallest faint star clusters known to date. Furthermore, using deeper imaging of DES J0222.7−5217 taken with the SOAR telescope, we update structural parameters and perform the first isochrone modeling. Our analysis yields the first age ($\simeq 12.6$ Gyr) and metallicity ($[\mathrm{Fe/H}] \simeq -2.01$) estimates for this object. The half-light radius ($r_\mathrm{h} \sim 10.5$ pc) and luminosity ($M_V \sim -2.7$) of DES J0222.7−5217 suggest that it is likely a faint star cluster. The discovery of DES 3 indicates that the census of stellar systems in the Milky Way is still far from complete, and demonstrates the power of modern wide-field imaging surveys to improve our knowledge of the Galaxy's satellite population.

Key words: Galaxy: halo – globular clusters: general.

1 INTRODUCTION

A fundamental prediction of the Lambda cold dark matter (ΛCDM) theory of structure formation is that galactic

---

⋆ **E-mail**: elmer.luque@ufrgs.br

This manuscript has been authored by Fermi Research Alliance, LLC under Contract No. DE-AC02-07CH11359 with the U.S. Department of Energy, Office of Science, Office of High Energy Physics.

DM haloes of the size of the Milky Way (MW) grow by the accretion of smaller sub-systems (e.g. White & Rees 1978; Davis et al. 1985; Font et al. 2011). The Sagittarius dwarf galaxy and the globular cluster Palomar 5 are interesting examples of physical systems that are even now going through the process of tidal disruption before being absorbed by the MW (see e.g. Ibata et al. 1994; Odenkirchen et al. 2002). Spectroscopic observations have shown that the dwarf galaxies are DM dominated systems, while there is virtually no evidence of DM halos surrounding the globular clusters (e.g. Willman & Strader 2012; Ibata et al. 2013).

Based on the horizontal branch (HB) morphology, metallicity, structure and kinematics, the globular clusters of the MW halo have been classified into two groups: the Young and Old Halo globular clusters (Zinn 1985, 1993; Mackey & Gilmore 2004; Mackey & van den Bergh 2005; Milone et al. 2014; Marino et al. 2014, 2015). It is established observationally that the accretion of dwarf galaxies leads to the accretion of globular clusters, the so-called Young Halo clusters, and possibly open clusters (e.g. Mackey & Gilmore 2004; Mackey & van den Bergh 2005; Carraro & Bensby 2009; Law & Majewski 2010, and references therein). Therefore, searching for star clusters can help us understand the assembly history of our Galaxy and the associated globular cluster system.

With the advent of the Sloan Digital Sky Survey (SDSS; York et al. 2000), a new class of star clusters was discovered (e.g. Koposov et al. 2007; Belokurov et al. 2010; Fadely et al. 2011; Muñoz et al. 2012; Kim & Jerjen 2015a). These star clusters have very low luminosities ($-3.0 \lesssim M_V \lesssim 0$), small half-light radii ($r_{\rm h} < 10\,{\rm pc}$), and are thought to suffer mass-loss via dynamical processes such as tidal disruption or evaporation (see e.g. Koposov et al. 2007; Kim & Jerjen 2015a). The census of MW satellite galaxies has also increased considerably, from 11 classical dwarfs known in 1990, up to a total of 27 that were known by early 2015 (McConnachie 2012). Over the past two years many satellite candidates have been found in the following surveys: the Dark Energy Survey (DES; The Dark Energy Survey Collaboration 2005), the Panoramic Survey Telescope and Rapid Response System 1 (Laevens et al. 2014, 2015a,b), the Survey of the Magellanic Stellar History (Martin et al. 2015), VST ATLAS (Torrealba et al. 2016a,b), the Hyper Suprime-Cam Subaru Strategic Program (Homma et al. 2016, 2017), and the Magellanic SatelLites Survey (Drlica-Wagner et al. 2016). In particular, 21 stellar system candidates with $M_V \gtrsim -8$ have been found in DES (Bechtol et al. 2015; Drlica-Wagner et al. 2015; Koposov et al. 2015a; Kim & Jerjen 2015b; Luque et al. 2016, 2017). Thus far, spectroscopic measurements of radial velocity and metallicity have confirmed that Reticulum II (Koposov et al. 2015b; Simon et al. 2015; Walker et al. 2015), Horologium I (Koposov et al. 2015b), Tucana II (Walker et al. 2016), Grus I (Walker et al. 2016), Tucana III (Simon et al. 2017), and Eridanus II (Li et al. 2017) are indeed dwarf galaxies. The possible association of the recently discovered DES dwarf galaxy candidates with Large and Small Magellanic Clouds (LMC and SMC) has been discussed by several authors (e.g. Bechtol et al. 2015; Drlica-Wagner et al. 2015, 2016; Koposov et al. 2015a; Jethwa et al. 2016; Dooley et al. 2017; Sales et al. 2017). Several of the candidates may be associated with the Sagittarius stream (Luque et al. 2017).

Here, we announce the discovery of a new MW star cluster, which we call DES 3, in the constellation of Indus. The object was detected as a stellar overdensity in the first internal release of the DES co-add data (Y1A1), which covers a solid angle of $\sim 1800\,{\rm deg}^2$ in the southern equatorial hemisphere, and later confirmed with deep SOAR imaging. We additionally present deeper imaging of DES J0222.7−5217 (Eridanus III) taken with the SOAR telescope in order to determine its properties, several of which have not been reported in the literature (Bechtol et al. 2015; Koposov et al. 2015a). We use these deeper data to better investigate the nature of this object, whether it be a star cluster or a very small faint dwarf. If DES J0222.7−5217 is confirmed to be a star cluster, it will be named DES 4. This paper is organized as follows. Section 2 describes the method used to search for star clusters and other stellar systems. In Section 3, we describe the first-year DES data and discovery of DES 3. The photometric follow-up observations and data reduction are presented in Section 4. In Section 5, we quantify the physical properties of the new stellar object. In Section 6, we present the updated properties of DES J0222.7−5217 with deeper imaging. Our final remarks are given in Section 7.

2 SUBSTRUCTURE SEARCH METHOD

Here we briefly review our overdensity search technique (SPARSEX; Luque et al. 2016). The SPARSEX code is based on the matched-filter (MF) method (Rockosi et al. 2002; Szabo et al. 2011). It minimizes the variance between star counts from a data catalogue and a model containing a simple stellar population (SSP) and a MW field star contamination. This minimization is carried out over colour and magnitude bins for each individual and small spatial cell. A grid of SSPs covering a wide range of ages, metallicities, and distances, is created using the code GENCMD[1]. The model of field stars is created from the catalogue data over $10^\circ \times 10^\circ$ regions, to account for possible variations in the field population mix. The variance minimization yields the SSP model normalization as a function of position, i.e., a map with the number density of stars consistent with that particular SSP. We then convolve each SSP map with different spatial kernels to highlight substructures of different sizes. For each of these maps, we apply SExtractor (Bertin & Arnouts 1996) to identify the most significant and/or frequently detected overdensities. Then we perform visual inspection on the images, colour-magnitude diagram (CMD) and significance profile of each candidate. The significance profile is defined as the ratio of the number of stars $N_{\rm obj}$ inside a given radius in excess of the number $N_{\rm bgd}$, relative to the expected fluctuation in the same field background, i.e, $N_{\rm obj}/\sqrt{N_{\rm bgd}}$. Defining $N_{\rm obs}$ to be the total number of observed stars, then $N_{\rm obj} = (N_{\rm obs} - N_{\rm bgd})$. To avoid a low stellar statistic, we built the significance profile using a cumulative radius of $1'$ centred on the candidate. $N_{\rm bgd}$ is computed within a circular annulus at $30' < r < 36'$ from each candidate. We refer

---

[1] https://github.com/balbinot/gencmd

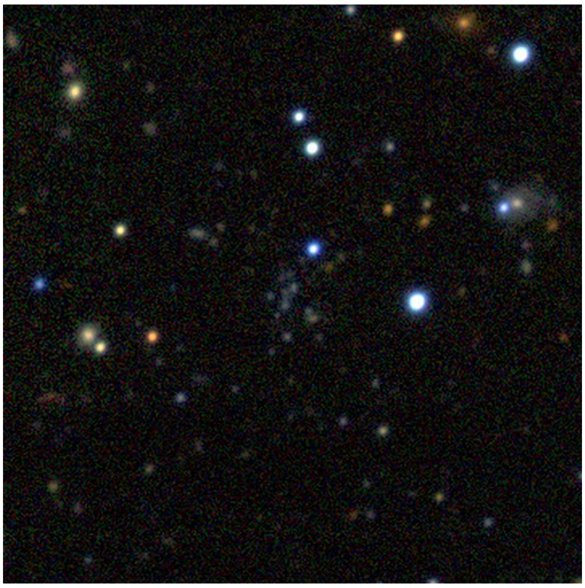

Figure 1. DES co-add image cutout of DES 3 taken from the DES Science portal. The 1.58 arcmin × 1.58 arcmin image is centred on DES 3. The R,G,B channels correspond to the i, r, g bands.

to Luque et al. (2016, 2017) and to Sections 3 and 5 below for more details.

3 DES DATA AND DISCOVERY

DES is a wide-field optical survey that uses the Dark Energy Camera (DECam; Flaugher et al. 2015) to image 5000 deg^2 in the southern equatorial hemisphere. DECam is an array of 62 2k × 4k CCDs, with pixel scale of $0\farcs263$, that images a $2\fdg2$ diameter field of view. It is installed at the prime focus of the 4-metre Blanco telescope at Cerro Tololo Inter-American Observatory. DECam images are reduced by the DES Data Management (DESDM) system. The pipeline consists of image detrending, astrometric calibration, nightly photometric calibration, global calibration, image coaddition, and object catalogue creation (see Sevilla et al. 2011; Desai et al. 2012; Mohr et al. 2012; Balbinot et al. 2015; Drlica-Wagner et al. 2017, for a more detailed description). The SExtractor toolkit is used to create catalogues from the processed and co-added images (Bertin & Arnouts 1996; Bertin 2011).

To search for stellar substructures in the DES Y1A1 catalogue, we applied cuts based on the SExtractor parameters `SPREAD_MODEL`, `FLAGS` and point spread function (`PSF`) magnitudes. The `FLAGS` parameter denotes if an object is saturated or has been truncated at the edge of the image and a cut of `FLAGS` < 4 is sufficient for our purposes. We apply this restriction in all our subsequent analyses. The `SPREAD_MODEL` parameter is the main star/galaxy separator. To avoid issues arising from fitting the `PSF` across variable-depth co-added images, we utilized the weighted-average (`WAVG`) of the `SPREAD_MODEL` measurements from the single-epoch exposures (see Bechtol et al. 2015). Therefore, our stellar sample consists of sources in the i band with |`WAVG_SPREAD_MODEL`| $< 0.003 +$ `SPREADERR_MODEL` as described in Drlica-Wagner et al. (2015) and Luque et al. (2016). In addition, magnitude[2] ($17 < g_{\rm DES} < 24$) and colour ($-0.5 < g_{\rm DES} - r_{\rm DES} < 1.2$) cuts were also applied. The colour cut was performed to exclude stars from the Galactic disc and possibly spurious objects that can contaminate our sample. Each star was extinction corrected from the reddening map of Schlegel et al. (1998).

Applying the method described in Section 2 on DES Y1A1 data, we have successfully recovered all ten stellar objects that have been reported in first-year DES data[3] (Bechtol et al. 2015; Koposov et al. 2015a; Kim & Jerjen 2015b; Luque et al. 2016). These detections include the faint satellite DES J0222.7−5217, which we detect with significance of 16.1σ. Bechtol et al. (2015) reported DES J0222.7−5217 with a heliocentric distance of 95 kpc, an absolute magnitude of -2.4 ± 0.6, and a half-light radius of 11^{+8}_{-5} pc. In contrast, Koposov et al. (2015a) found DES J0222.7−5217 to be slightly less distant, 87 kpc, with an absolute magnitude of -2.0 ± 0.3, and a half-light radius of $14.0^{+12.5}_{-2.6}$ pc. Deeper imaging is necessary to conclusively determine the characteristics of this faint satellite.

In addition, to the previously detected satellites, we detected one new star cluster, DES 3, with a statistical significance of 8.3σ. DES 3 is readily visible as a cluster of faint blue stars in the DES co-add images[4] (see Fig. 1). The fact that they are blue sources indicates that this overdensity is not a galaxy cluster. The overdensity is also clear from the DES stellar map shown in panel (a) of Fig. 2. For comparison, in panel (b), we show the density map of sources classified as galaxies. Note that faint galaxies do not contribute to the observed overdensity of DES 3. In panel (c) of Fig. 2, the circular significance profile is shown. Note that the significance profile shows the higher peak at $r = 1'$ from the centre of DES 3, where $N_{\rm obj} = 22$ and $N_{\rm bgd} = 7$ stars. To take into account the missing coverage[5] observed in panels (a) and (b) of Fig. 2, in this analysis, we estimated the effective area ($A_{\rm eff}$) for each circular region as follows. After inserting a certain number of uniformly distributed random points (N) inside a circle with radius r centred on DES 3, we computed the ratio between the number of points that fall inside the region of the sky that is covered by the DES data ($N_{\rm in}$) and N. Therefore, for each region $A_{\rm eff} = A\frac{N_{\rm in}}{N}$, where A is the area of the circle.

In panel (d) of Fig. 2, we show the CMD of DES 3 constructed with stars within a circle of radius $r = 0\farcm6$. We also have plotted a PARSEC (CMD v3.0;[6] Bressan et al. 2012) isochrone model (solid line) corresponding to the best-fitting parameters (this will be discussed fully in Section 5). There are stars with $g_{\rm DES} \gtrsim 22.5$ mag scattered in the CMD, some

---

[2] We refer the `WAVG_MAG_PSF` measurements in the DES gri filters as $g_{\rm DES}$, $r_{\rm DES}$ and $i_{\rm DES}$, respectively.

[3] The eleventh object, Grus 1, reported by Koposov et al. (2015a) is in a region of Y1 data that is not included in the Y1A1 coadd due to limited coverage in some of the DES filters.

[4] The images were taken from the DES Science portal. The latter is a web-based system being developed by DES-Brazil and Laboratório Interinstitucional de e-Astronomia (LIneA, http://www.linea.gov.br) for the DES collaboration.

[5] We masked the regions on the sky where there is absence of sources.

[6] We are using PARSEC isochrones revised to include instrumental and atmosphere response.

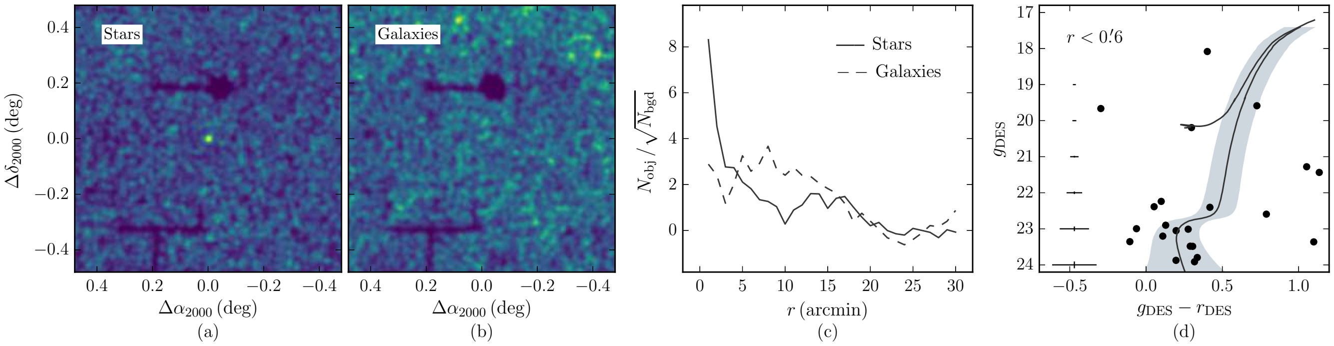

Figure 2. Detection of DES 3 from the DES data. Panel (a): stellar density map around DES 3. Panel (b): similar to previous panel, but now for galaxies. Panel (c): significance profile as a function of radius r from the centre of DES 3. The solid line corresponds to stars, while the dashed line corresponds to galaxies. Panel (d): CMD of stars within a circle with radius $r = 0\overset{\prime}{.}6$ from the centre of DES 3. A PARSEC (solid line) isochrone model with age 9.8 Gyr and [Fe/H] $= -1.88$ is overplotted at a distance of 76.2 kpc (see Section 5 for details of the best-fitting isochrone). The isochrone filter (gray shaded area) based on photometric uncertainties contains the most likely members. The mean photometric errors in both colour and magnitude are shown in the extreme left of this panel.

of which fall inside the isochrone filter[7] (gray shaded area). We are tempted to say that these stars belong to the main sequence turn-off (MSTO) and sub-giant branch (SGB) of DES 3. Note that the CMD also shows one star that may belong to the HB. However, based on the limited information given by this CMD, we are not able to confirm the nature and infer reliable parameters for DES 3. In order to reach the main sequence (MS; $g_{\rm DES} \sim 25.5$ mag) in the CMD, deeper follow-up observations are required.

4 SOAR FOLLOW-UP DATA

Follow-up imaging of DES 3 and DES J0222.7−5217 was carried out on 2016 July 29 and October 20 respectively, using the SOAR Optical Imager (SOI) on the 4.1-metre Southern Astrophysical Research (SOAR) telescope. SOI consists of two 2048×4096 CCDs and covers a $5\overset{\prime}{.}2 \times 5\overset{\prime}{.}2$ field. The SOI CCDs have a scale of $0\overset{\prime\prime}{.}077$/pixel. As the images were binned 2×2, the final image scale is $0\overset{\prime\prime}{.}154$/pixel. We observed each object for a total of 45 min in each SDSS filter (g and r; hereafter g' and r'). The integrations were split into nine exposures of 300 s to avoid overexposing. The observations were carried out with an airmass below 1.20.

Raw exposures were trimmed, corrected for bias, and flat fielded by the SOAR Brazilian Resident Astronomers, David Sanmartin and Luciano Fraga, using SOAR/IRAF packages. Individual exposures for each filter, g' and r', were coadded. In particular, Fig. 3 shows the SOAR/SOI (g' band only) coadded images of DES 3. The figure attests to the increase in spatial resolution[8] and in photometric depth when the latter is compared with the DES images (see Fig. 1). The scattered light observed in Fig. 3 is discussed in the text below. To create a source catalogue in the direction of DES 3 and DES J0222.7−5217, we use a combination of the SExtractor/PSFEx routines (Bertin & Arnouts 1996; Bertin 2011). A first pass of SExtractor is run to create an input catalogue for PSFEx. The PSFEx routine creates a `PSF` image for a second pass of SExtractor that determines the `PSF` magnitude and the `SPREAD_MODEL` parameter.

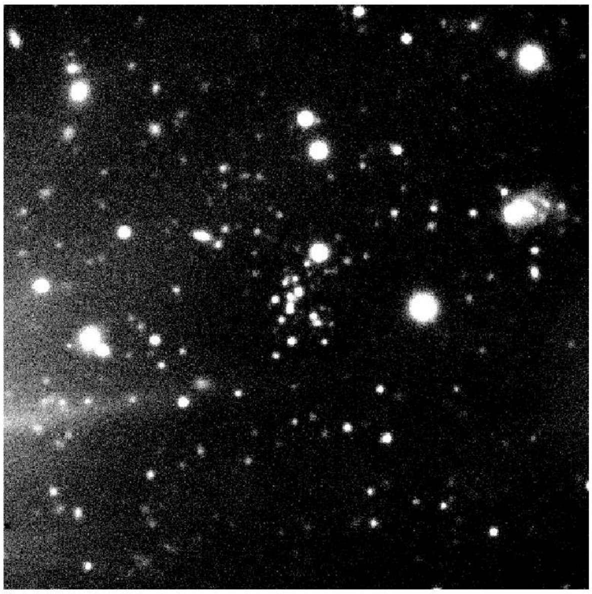

Figure 3. SOAR g band co-add image cutout of DES 3. The 1.58 arcmin × 1.58 arcmin image is centred on DES 3.

We transformed the instrumental magnitudes, $g_{\rm inst}$ and $r_{\rm inst}$, to apparent magnitudes[9], g and r, by using a set of DES stars in the direction of each object. This process was performed as follows: first we built a SOAR catalogue by merging the g' and r' full photometric lists, using a match-

---

[7] The isochrone filter is built by using the photometric uncertainties in both colour and magnitude. We added a value of 0.1 mag in the colour-magnitude space to avoid too narrow isochrone filters at the bright magnitudes, where the uncertainties are small (for details, see Luque et al. 2016).

[8] By using several bright and isolated stars in the direction of DES 3, we determined that the DES co-added images have an average `PSF` FWHM of $\simeq 1\overset{\prime\prime}{.}19$ and $0\overset{\prime\prime}{.}94$ in the g and r bands, respectively, while the SOAR co-added images have a value of $\simeq 0\overset{\prime\prime}{.}8$ in both g' and r' bands.

[9] The $g_{\rm inst}$ and $r_{\rm inst}$ magnitudes are given by $-2.5 \times \log(\text{counts})$, while the g and r magnitudes correspond to $g_{\rm DES}$ and $r_{\rm DES}$, respectively.

Table 1. Calibration coefficients obtained from the fit of the set of equations presented in equation 1.

Coefficient	DES 3	DES J0222.7−5217
β (mag)	31.71 ± 0.02	31.43 ± 0.08
γ	-0.10 ± 0.02	-0.16 ± 0.09
ζ (mag)	31.70 ± 0.02	31.51 ± 0.03
η	-0.15 ± 0.03	-0.12 ± 0.02

ing radius of $0\overset{\prime\prime}{.}5$. We also selected DES stellar sources with |`WAVG_SPREAD_MODEL`| < 0.003 and `WAVG_MAGERR_PSF` < 0.03 to obtain a sufficiently pure stellar sample. Next, we matched the SOAR sources with DES brightest (from 17 to 22 mag) stars, on g' and r' filters, using a radial tolerance of $0\overset{\prime\prime}{.}5$. Then, we use these brightest stars to fit the following calibration curves:

$$
\begin{aligned}
g &= g_{\rm inst} + \beta + \gamma(g_{\rm DES} - r_{\rm DES}), \\
r &= r_{\rm inst} + \zeta + \eta(g_{\rm DES} - r_{\rm DES}),
\end{aligned}
\tag{1}
$$

where the β and ζ coefficients represent the zero points of the two bands, while γ and η are the colour term coefficients. Airmass correction, in both filters, was assumed to be constant and, therefore, it is absorbed by the zero point coefficient. The results of our fits are presented in Table 1. Estimates for the two objects are identical within uncertainties. The calibration was then applied to all instrumental magnitudes in the photometric list. Finally, all magnitudes of the calibrated sources were corrected for Galactic reddening using the Schlegel et al. (1998) dust maps.

For our further analysis, we modify the cuts to reach faint magnitudes. Our stellar sample consists of sources with |`SPREAD_MODEL`| $< 0.003 +$ `SPREADERR_MODEL`. Moreover, we applied colour ($-0.5 < g_{\rm DES} - r_{\rm DES} < 1.2$) and magnitude ($g_{\rm DES} > 17$) cuts. The faint $g_{\rm DES}$ magnitude, for each catalogue, is established based on the magnitude error (σ_g), where σ_g has a value of ≈ 0.07 mag. Therefore, this limiting magnitude corresponds to $g_{\rm DES} < 25$ ($g_{\rm DES} < 24.5$) for the star catalogue in the direction of DES 3 (DES J0222.7−5217).

We have verified that the scattered light observed only in the DES 3 images (see Fig. 3) does not affect the completeness of sources (stars and galaxies) down to a magnitude depth $g_{\rm DES} \sim 25$ mag. To check we count sources as a function of magnitude both inside and outside scattered light affected regions. These regions have equal areas, which contain 159 and 154 sources, respectively. Thus, we find that both counts of sources in function of the magnitude are similar.

The completeness of our photometry has been evaluated performing artificial star tests on the SOAR images. The completeness curves are constructed with reference to the centre of each object up to an external radius $r = 1'$, taking regular intervals of $\Delta r = 0\overset{\prime}{.}1$. Artificial stars from 20th to 27th magnitudes in steps of 0.5 mag were added to the same image with the IRAF/ADDSTAR routine using a `PSF` model derived from several bright and isolated stars. In order to avoid the crowding in the images, only 15 per cent of the original number of sources (stars and galaxies) detected in each region were added per run[10]. After inserting the artificial stars, these artificial images were reduced with the same SExtractor/PSFEx routines as the SOAR images. SExtractor/PSFEx assigns each detected object a `SPREAD_MODEL` value. We consider point source candidates those sources with |`SPREAD_MODEL`| $< 0.003 +$ `SPREADERR_MODEL` (see text above for details). At last, the artificial stars are considered to be recovered if the input and output positions are closer than $0\overset{\prime\prime}{.}5$, and magnitude differences are less than 0.5 mag. The completeness curves as a function of magnitude and distance from the centre of DES 3 are shown in Fig. 4.

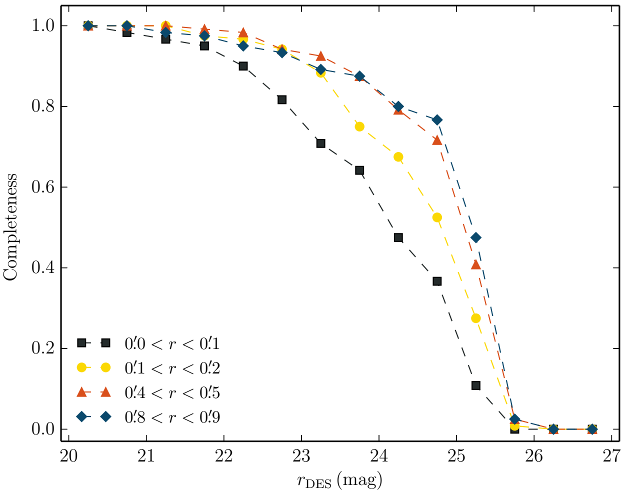

Figure 4. Completeness curves as function of magnitude and radius from the SOAR data. The solid squares represent the completeness at a radius of $0\overset{\prime}{.}1$ from the centre of DES 3, the solid dots represent the completeness within an annulus with radius $0\overset{\prime}{.}1 < r < 0\overset{\prime}{.}2$, the solid triangles represent the completeness within an annulus with radius $0\overset{\prime}{.}4 < r < 0\overset{\prime}{.}5$, and the solid diamonds represent the completeness within an annulus with radius $0\overset{\prime}{.}8 < r < 0\overset{\prime}{.}9$.

5 PROPERTIES OF DES 3

In order to better constrain the properties and the nature of DES 3, we use SOAR data, which is ~ 1 mag deeper than the DES data in the region of this stellar object (see Fig. 3).

We use the maximum likelihood method to determine the structural and CMD parameters for DES 3. We used the EMCEE[11] Python package (Foreman-Mackey et al. 2013), which implements an affine invariant Markov Chain Monte Carlo (MCMC) ensemble sampler, to sample the ln–likelihood function over the parameter space. We have assumed flat priors for all parameters. We take the median of each marginalized posterior distribution function (PDF) to be the best-fitting solution, with uncertainties given by the 16th and 84th percentiles, equivalent to $\pm 1\sigma$ assuming the PDFs are normal distributions.

---

[10] After multiple runs, we obtained a total of 120 artificial stars in each bin of magnitude.

[11] http://dan.iel.fm/emcee/current/

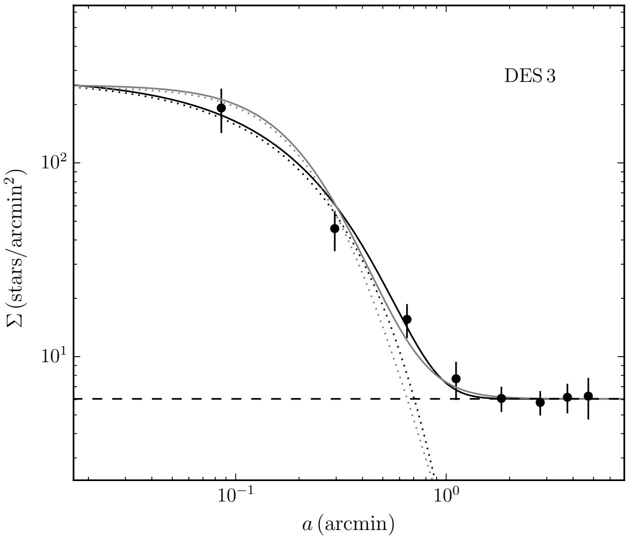

Figure 5. Filled points show a binned version of the density profile of DES 3, constructed in elliptical annuli using the derived structural parameters from the best-fitting exponential profile (see Table 2). The error bars are 1σ Poisson uncertainties. The gray (black) dotted line represent the best-fitting of Plummer (exponential) profile. The horizontal dashed line shows the field background level. The gray (black) solid line is the combination of the background level with the Plummer (exponential) profile.

Table 2. Properties of DES 3.

Parameters	Exponential profile	Plummer profile	Unit
α_0 ($J2000$)	$21\ 40\ 13.27^{+0.09}_{-0.09}$	$21\ 40\ 13.20^{+0.11}_{-0.11}$	h m s
δ_0 ($J2000$)	$-52\ 32\ 31.20^{+1.50}_{-1.50}$	$-52\ 32\ 30.48^{+1.62}_{-1.68}$	$^\circ\ '\ ''$
l	343.83	343.83	deg
b	-46.51	-46.51	deg
$D_\odot$	$76.2^{+2.8}_{-4.9}$	$76.2^{+3.2}_{-5.3}$	kpc
r_h	$0.31^{+0.04}_{-0.03}$	$0.28^{+0.04}_{-0.03}$	arcmin
r_h	$6.87^{+0.92\,a}_{-0.80}$	$6.21^{+0.92\,a}_{-0.79}$	pc
θ	$-47.0^{+31.1}_{-32.8}$	$-34.9^{+28.8}_{-25.7}$	deg
ϵ	$0.13^{+0.12}_{-0.09}$	$0.17^{+0.13}_{-0.11}$	
$\Sigma_{\rm bgd}$	6.1 ± 0.5	6.1 ± 0.5	$\frac{\rm stars}{\rm arcmin^2}$
M_V	$-1.8^{+0.4}_{-0.3}$	$-2.0^{+0.4}_{-0.3}$	mag
[Fe/H]	$-1.88^{+0.17}_{-0.13}$	$-1.88^{+0.22}_{-0.15}$	dex
Age	$9.8^{+1.4}_{-1.1}$	$9.8^{+1.4}_{-1.1}$	Gyr
$(m - M)_0$	$19.41^{+0.08}_{-0.14}$	$19.41^{+0.09}_{-0.15}$	mag

Note. ^{a}Adopting a distance of 76.2 kpc.

To estimate the structural parameters, we follow a convention similar to that of Martin et al. (2008). We adopt two different density profile models: exponential and Plummer (Plummer 1911). Due to the small field covered by the SOAR/SOI images, we parameterize both models with just five free parameters. For the exponential profile, the free parameters are: central coordinates α_0 and δ_0, position angle θ, ellipticity ϵ and exponential scale radius r_e. For the Plummer profile, the parameters are: α_0, δ_0, θ, ϵ and Plummer scale radius r_p. The exponential scale radius is related to the half-light radius by the relation $r_h = 1.68 r_e$, whereas the Plummer scale radius, r_p, is equivalent to r_h. The background density, $\Sigma_{\rm bgd}$, is determined by using a region outside $r > 1\farcm5$ around DES 3, which results in 6.1 $\frac{\rm stars}{\rm arcmin^2}$, and it is kept constant in the fits.

Fig. 5 shows the binned elliptical density profile of DES 3. To determine the effective area of each elliptical annulus, correcting for the gap and borders of the field covered by the SOI CCDs, we follow the same technique used in Section 3. The best-fitting exponential and Plummer models are also overplotted in this figure. As it can be seen, both the exponential and Plummer profiles adequately describe the observed data. From both models, we find that DES 3 is only slightly elongated ($\epsilon \sim 0.15$) and compact, with a half-light radius of $r_h \sim 0\farcm3$. Its ellipticity is very similar to Kim 2 ($\epsilon \simeq 0.12$; Kim et al. 2015) and Kim 3 ($\epsilon \simeq 0.17$; Kim et al. 2016a). Only Koposov 1 and Koposov 2, with $r_h \sim 0\farcm21$ and $r_h \sim 0\farcm26$, respectively (Koposov et al. 2007), have slightly smaller apparent angular sizes than DES 3. The set of structural parameters for DES 3 is presented in Table 2.

For CMD fits, we first weight each star by the membership probability p taken from the best profile fits. We then selected all the stars with a threshold of $p \geqslant 0.01$ to fit an isochrone model. The free parameters age, $(m - M)_0$ and metallicity[12], Z, are simultaneously determined by this fitting method (Luque et al. 2016, 2017; Pieres et al. 2016). To investigate a possible range in the CMD parameters, in this analysis we use the selected stars from both exponential and Plummer models.

In the left panel of Fig. 6, we show the CMD of DES 3 from the SOAR data. We show only stars within an ellipse with semimajor axis $a \sim 2r_h$ according to the best-fitting exponential profile (see Table 2). This CMD clearly shows the presence of MS and SGB stars down to $g_{\rm DES} \simeq 25.5$. We can also identify one star that may belong to the HB. In the middle panel of Fig. 6, we show the CMD of background stars contained in an elliptical annulus, centred on DES 3, of equal area as the previous panel, whose inner semimajor axis is equal to $a = 2'$. We used the technique described in Section 3 to determine the effective area of this region. The excess of stars within the isochrone filter seen in the left panel relative to the background is remarkable, attesting not only the physical reality of DES 3, but also allowing a detailed CMD analysis. For comparison, in the right panel of this figure, we show the CMD of DES 3 from the DES data (see right panel of Fig. 2). As expected, the SOAR-based CMD is substantially more informative.

By using the maximum-likelihood method to fit the CMD distribution, we find that DES 3 population is well described by a PARSEC (Bressan et al. 2012) isochrone model with age 9.8 Gyr, $(m - M)_0 \simeq 19.41$, and $[{\rm Fe/H}] \simeq -1.88$. These parameters agree for both density profile models (exponential and Plummer). This is not surprising given that these models adequately describe the observed density profile of DES 3 (see Fig. 5). The best-fitting isochrone is overplotted in each panel of Fig. 6 as the solid line. In the same figure, an isochrone filter (gray shaded area) is also shown in each panel.

The absolute magnitude (M_V) has been determined using a similar approach as Koposov et al. (2015a). We integrate over all masses along the best-fitting model isochrone

---

[12] We adopted $Z_\odot = 0.0152$ (Bressan et al. 2012) in order to convert from Z to [Fe/H], assuming $[{\rm Fe/H}] = \log(Z/Z_\odot)$.

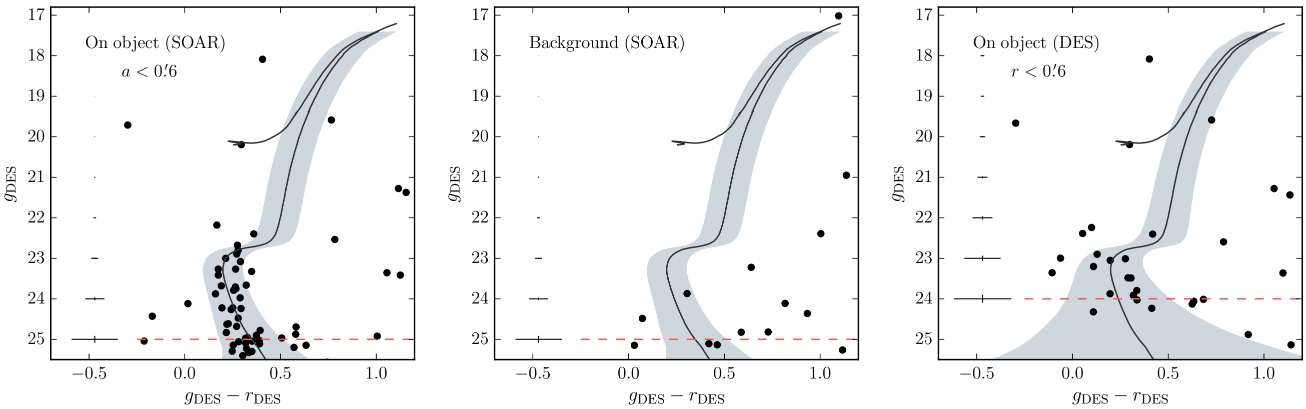

Figure 6. Left panel: CMD of DES 3 from the SOAR data. Only stars inside an ellipse with semi-major axis $a \sim 2r_{\rm h}$ from the centre of DES 3 are shown. In this and the other two panels, the best-fitting PARSEC (Bressan et al. 2012) isochrone derived from the SOAR data is shown. The isochrone filter (gray shaded area) based on photometric uncertainties contains the most likely members. Middle panel: CMD of field stars in an elliptical annulus of equal area on the sky as the previous panel. Right panel: CMD of DES stars within a radius $r = 0.'6$ centred on DES 3. The horizontal dashed line in each panel indicates the faint magnitude limit used. The mean photometric errors in both colour and magnitude are shown in the extreme left of each panel.

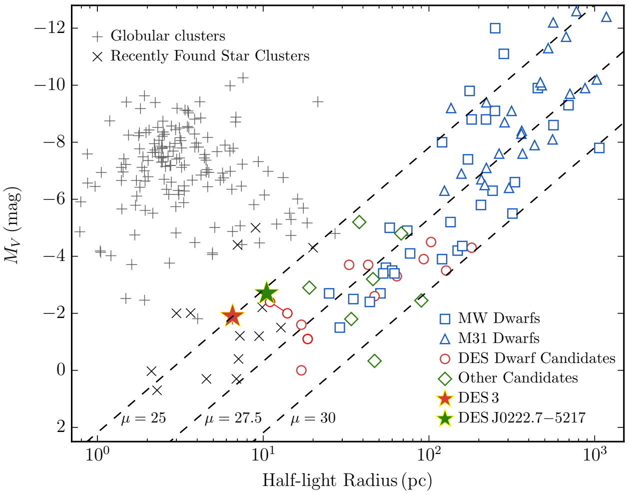

Figure 7. Absolute magnitude as a function of half-light radius. MW globular clusters ('+' symbols; Harris 2010), recently found MW star clusters ('×' symbols; Koposov et al. 2007; Belokurov et al. 2010; Muñoz et al. 2012; Balbinot et al. 2013; Laevens et al. 2014, 2015b; Kim & Jerjen 2015a; Kim et al. 2015, 2016a; Luque et al. 2016, 2017; Koposov et al. 2017), MW dwarf galaxies (blue squares; McConnachie 2012; Bechtol et al. 2015, Drlica-Wagner et al. 2015; Koposov et al. 2015a; Kim et al. 2016b; Torrealba et al. 2016a,b), M 31 dwarf galaxies (blue triangles; McConnachie 2012), previously reported dwarf galaxy candidates in the DES footprint (red circles; Bechtol et al. 2015; Drlica-Wagner et al. 2015; Koposov et al. 2015a; Kim & Jerjen 2015b; Luque et al. 2017), other recently reported dwarf galaxy candidates (green diamonds; Laevens et al. 2015a,b; Martin et al. 2015; Drlica-Wagner et al. 2016; Homma et al. 2016, 2017), DES 3 (red star), and DES J0222.7−5217 (green star) are shown. The red circles connected with a line represent the two previous DES J0222.7−5217 estimates. Note that DES 3 and DES J0222.7−5217 lie inside the region inhabited by faint star clusters. The uncertainties of both objects are comparable to the symbol size. The dashed lines indicate contours of constant surface brightness at $\mu = \{25, 27.5, 30\}$ mag arcsec^{-2}.

assuming a Kroupa (2001) initial mass function, and normalize the number of objects by those observed in the CMD with $r_{\rm DES} < 24.5$ mag and which fall in the isochrone filter. For this estimate, we selected all stars with a membership threshold of $p \geqslant 0.01$ taken from the best profile fits. We corrected the star counts for completeness by weighting each star by $w_i = 1/c_i$, where c_i is the completeness of the star interpolated in magnitude for an interval of radius (see Fig. 4). Due to the low number of objects observed in this type of objects, the estimate of the absolute magnitude has large uncertainty. We then calculate the uncertainty by estimating the upper and lower limits for the integrated V magnitude. We convert the $g_{\rm DES}$ and $r_{\rm DES}$ magnitudes to V magnitude using a SDSS stellar calibration sample[13] and the equation from Jester et al. (2005),

$$\begin{aligned} g_{\rm DES} &= g_{\rm SDSS} - 0.075(g_{\rm SDSS} - r_{\rm SDSS}) + 0.001 \\ r_{\rm DES} &= r_{\rm SDSS} - 0.069(g_{\rm SDSS} - r_{\rm SDSS}) - 0.009 \qquad (2) \\ V &= g_{\rm SDSS} - 0.59(g_{\rm SDSS} - r_{\rm SDSS}) - 0.01. \end{aligned}$$

This procedure yields an absolute magnitude of $M_V = -1.8^{+0.4}_{-0.3}$ for the exponencial model and $M_V = -2.0^{+0.4}_{-0.3}$ for the Plummer model. Therefore, in the size-luminosity plane DES 3 lies in the faint star cluster region (see Fig. 7). The luminosity of DES 3 is comparable to Koposov 1 ($M_V \sim -2$; Koposov et al. 2007), DES 1 ($M_V \sim -2.21$; Luque et al. 2016), and Gaia 2 ($M_V \simeq -2$; Koposov et al. 2017). However, the small size ($r_{\rm h} \sim 6.5$ pc) of DES 3 is comparable to Balbinot 1 ($r_{\rm h} \simeq 7.24$ pc; Balbinot et al. 2013), Kim 1 ($r_{\rm h} \simeq 6.9$ pc; Kim & Jerjen 2015a) and Laevens 3 ($r_{\rm h} \simeq 7$ pc; Laevens et al. 2015b).

---

[13] This new version of transformation equations are based on SDSS Data Release 13 (DR13) and DES Year 3 Annual Release (Y3A1) single-epoch data.

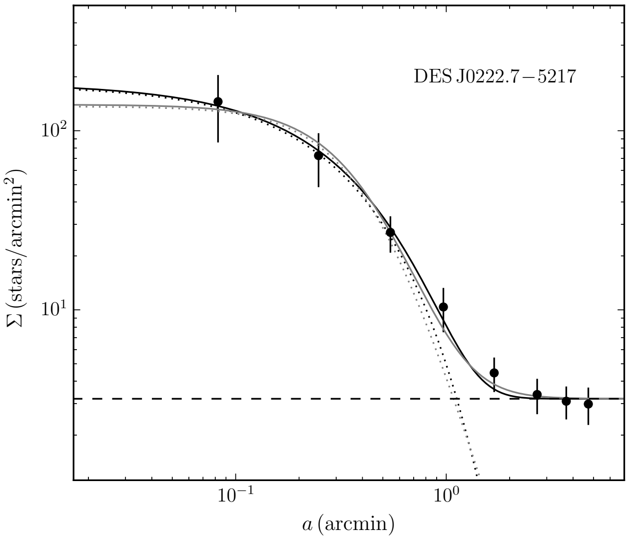

Figure 8. Elliptical surface density profile of DES J0222.7−5217. The filled points represent the observed values with 1σ error bars. The gray (black) dotted line represents the best-fitting of Plummer (exponential) profile. The horizontal dashed line represents the background density. The gray (black) solid line is the combination of the background level with the Plummer (exponential) profile.

Table 3. Properties of DES J0222.7−5217.

Parameters	Exponential profile	Plummer profile	Unit
α_0 ($J2000$)	$02\ 22\ 45.46^{+0.16}_{-0.19}$	$02\ 22\ 45.56^{+0.20}_{-0.20}$	h m s
δ_0 ($J2000$)	$-52\ 17\ 06.00^{+1.44}_{-1.44}$	$-52\ 17\ 06.06^{+1.38}_{-1.38}$	$^\circ\ '\ ''$
l	274.96	274.96	deg
b	−59.60	−59.60	deg
$D_\odot$	$77.6^{+2.1}_{-3.2}$	$77.6^{+2.1}_{-2.9}$	kpc
r_h	$0.47^{+0.06}_{-0.05}$	$0.46^{+0.06}_{-0.05}$	arcmin
r_h	$10.61^{+1.38\,a}_{-1.21}$	$10.38^{+1.38\,a}_{-1.19}$	pc
θ	$-83.2^{+6.7}_{-6.2}$	$-84.6^{+6.1}_{-5.6}$	deg
ϵ	$0.52^{+0.07}_{-0.09}$	$0.53^{+0.07}_{-0.09}$	
$\Sigma_{\rm bgd}$	3.2 ± 0.4	3.2 ± 0.4	$\frac{\rm stars}{\rm arcmin^2}$
M_V	$-2.6^{+0.5}_{-0.3}$	$-2.8^{+0.4}_{-0.3}$	mag
[Fe/H]	$-2.01^{+0.38}_{-0.12}$	$-2.01^{+0.23}_{-0.12}$	dex
Age	$12.6^{+0.6}_{-0.6}$	$12.6^{+0.3}_{-0.6}$	Gyr
$(m-M)_0$	$19.45^{+0.06}_{-0.09}$	$19.45^{+0.06}_{-0.08}$	mag

Note. ^{a}Adopting a distance of 77.6 kpc.

6 PROPERTIES OF DES J0222.7−5217

We obtained deeper photometric data for DES J0222.7−5217 with the SOAR telescope. Much like our SOAR imaging of DES 3, our SOAR imaging of DES J0222.7−5217 is $\sim$ 1 mag deeper than the DES data. We apply the same methodology described in Section 5 to provide updated properties of DES J0222.7−5217.

Fig. 8 shows the binned elliptical density profile of DES J0222.7−5217 and the best-fitting exponential and Plummer models. We find that the two models yield very similar structural parameters for this object (see Table 3). Our half-light radius ($r_h \sim 0'.47$) estimate is $\sim$ 12 per cent larger than the value determined by Bechtol et al. (2015, $r_h \simeq 0'.42$), but it is $\sim$ 13 per cent smaller than that determined by Koposov et al. (2015a, $r_h \simeq 0'.54$). We find the system to be more elliptical ($\epsilon \sim 0.53$) and less rotated ($\theta \sim -84$ deg) when compared to the values previously determined ($\epsilon \simeq 0.27$ and $\theta \simeq -97$ deg; Koposov et al. 2015a). In general, our results are in agreement within 1σ with the literature. However, our deeper data has allowed us to better constrain the structural parameters of DES J0222.7−5217 thereby reducing significantly the uncertainties reported in previous work.

The CMD of DES J0222.7−5217 from the SOAR data is shown in the left panel of Fig. 9. The CMD, built with stars within an elliptical annulus of semimajor axis $a \sim 2r_h$ centred on the object, clearly shows MS, MSTO, blue straggler (BS), red giant branch (RGB), and HB stars. Note that there is a potential asymptotic giant branch (AGB) star. The middle panel of Fig. 9 shows the CMD of field stars contained in an elliptical annulus of equal area as the previous panel, whose inner semimajor axis is $a = 2'.5$. For comparison, in the right panel of Fig. 9, we show the CMD of stars within $r = 0'.9$ of the centre of DES J0222.7−5217 from the DES data. Much like SOAR data, this CMD shows BS, RGB, HB, and AGB stars, however, it does not provide enough information about the MSTO and MS stars. Therefore, the SOAR CMD is substantially more informative than the DES CMD.

The best-fitting model isochrone, determined from the our CMD fit method, estimates that DES J0222.7−5217 is located at a distance of $D_\odot \simeq 77.6$ kpc and its stellar population is old ($\simeq$ 12.6 Gyr) and metal-poor ([Fe/H] $\simeq -2.01$). Again, the values of these parameters are consistent for both density profile models (see Table 3).

There is a moderate discrepancy between our heliocentric distance estimate and previous estimates of $D_\odot \simeq 95$ kpc (Bechtol et al. 2015) and $D_\odot \simeq 87$ kpc (Koposov et al. 2015a). In fact, this discrepancy may be due mainly to the limiting magnitude used in this work and those used by Bechtol et al. (2015) and Koposov et al. (2015a), since the resolution of the MS and MSTO allows for an improved distance measurement and estimations of the age and metallicity. Unfortunately, the metallicity and age values were not reported by these authors.

We estimate an absolute magnitude for DES J0222.7−5217 of $M_V = -2.6^{+0.5}_{-0.3}$ for the exponential profile and $M_V = -2.8^{+0.4}_{-0.3}$ for the Plummer profile. For these determinations, we used stars brighter than $r_{\rm DES}$ = 24 mag and the star counts were corrected for sample incompleteness. These results are in agreement (within 1σ) with those previously reported in the literature, $M_V \simeq -2.4$ (Bechtol et al. 2015) and $M_V \simeq -2.0$ (Koposov et al. 2015a).

With a half-light radius of $r_h \sim 10.5$ pc and a luminosity of $M_V \sim -2.7$, DES J0222.7−5217 lies in a region of size-luminosity space occupied by faint star clusters (see Fig. 7). Interestingly, the half-light radius, ellipticity and absolute magnitude of DES J0222.7−5217 are comparable to those for the star cluster DES 1 ($r_h \simeq 9.88$ pc, $\epsilon \simeq 0.53$ and $M_V \simeq -2.21$; Luque et al. 2016).

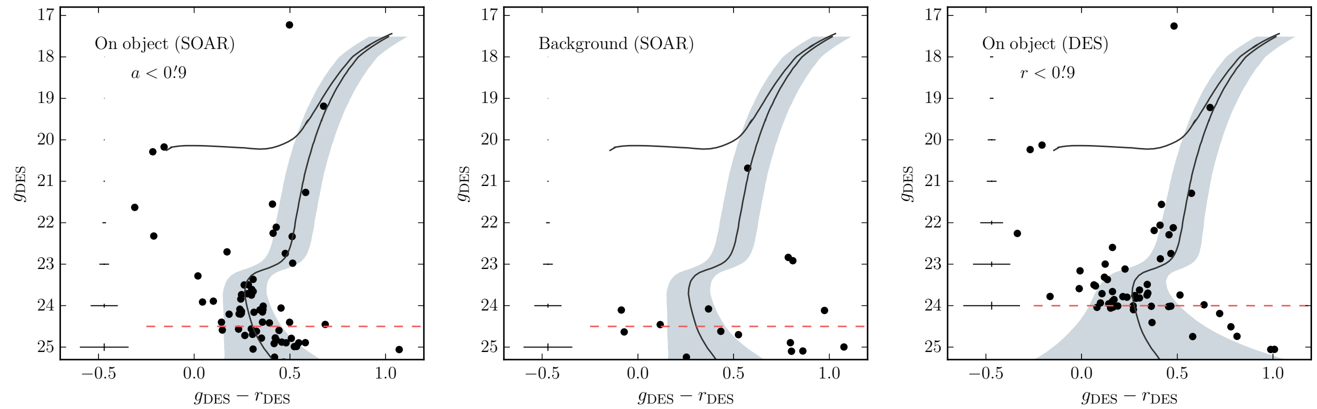

Figure 9. Left panel: CMD of DES J0222.7−5217 from the SOAR data. Only stars inside an ellipse with semi-major axis $a \sim 2r_{\rm h}$ from the centre of DES J0222.7−5217 are shown. In this and the other two panels, the best-fitting PARSEC (Bressan et al. 2012) isochrone derived from the SOAR data is shown. The isochrone filter (gray shaded area) based on photometric uncertainties contains the most likely members. Middle panel: CMD of field stars in an elliptical annulus of equal area on the sky as the previous panel. Right panel: CMD of DES stars within a circle with radius $r = 0\farcm9$ from the centre of DES J0222.7−5217. The horizontal dashed line in each panel indicates the faint magnitude limit used. The mean photometric errors in both colour and magnitude are shown in the extreme left of each panel.

7 CONCLUSIONS

In this paper, we announce the discovery of a new MW faint star cluster found in DES Y1A1 data, which we name DES 3. Its confirmation as a physical system required deep photometric imaging from the SOAR telescope. This new object adds to the 21 systems that have been found in the first two years of DES (Bechtol et al. 2015; Drlica-Wagner et al. 2015; Koposov et al. 2015a; Kim & Jerjen 2015b; Luque et al. 2016, 2017).

With a MCMC technique and two different density profile models (exponential and Plummer), we find that DES 3 is compact ($r_{\rm h} \sim 0\farcm3$) and slightly elongated ($\epsilon \sim 0.15$). The morphology of DES 3 does not suggest any evidence of on-going tidal disruption.

By means of an isochrone fit, we derive a distance of $\simeq 76.2$ kpc for DES 3. It is consistent with being dominated by an old ($\simeq 9.8$ Gyr) and metal-poor ([Fe/H] $\simeq -1.88$) population, as commonly observed in MW GCs found in the Galactic halo. However, its small physical size ($r_{\rm h} \sim 6.5$ pc) and low luminosity ($M_V \sim -1.9$) place DES 3 in the region occupied by faint star clusters as observed in Fig. 7. In fact, DES 3 is also one of the faint star clusters with smallest angular size known so far.

With deep SOAR data we found that DES J0222.7−5217 is located at a heliocentric distance of 77.6 kpc, and it hosts an old ($\simeq 12.6$ Gyr) and metal-poor ([Fe/H] $\simeq -2.01$) stellar population. Our best-fitting structural parameters for DES J0222.7−5217 are in general agreement (within 1σ) with the ones derived by Bechtol et al. (2015) and Koposov et al. (2015a), although the heliocentric distance determined in this work points to a closer object than previously reported. The half-light radius ($r_{\rm h} \sim 10.5$ pc) and luminosity ($M_V \sim -2.7$) of DES J0222.7−5217 suggest that it could be classified as a faint star cluster. However, the spectroscopic determination of the radial velocity of DES J0222.7−5217 will be very useful to confirm its nature.

Based on the Magellanic Stream (MS; Nidever et al. 2008) coordinates of DES 3, $(L_{\rm MS}, B_{\rm MS}) = -37\fdg39, -31\fdg69$ and DES J0222.7−5217, $(L_{\rm MS}, B_{\rm MS}) = -26\fdg45, 8\fdg25$, it is interesting to note that DES J0222.7−5217 is in a region where there is a high probability of finding objects associated with the Magellanic Clouds, while DES 3 lies close to a sequence of faint dwarf galaxies, some of which may also be associated with the Clouds (Fig. 10; Jethwa et al. 2016). However, DES 3 lies outside ±20° of the plane of the Magellanic Stream where the satellites of the LMC would be distributed (Jethwa et al. 2016).

Finally, the discovery of DES 3 in DES data indicates that the census of stellar systems, with characteristics of faint star clusters, is still incomplete. It is likely that additional new stellar systems will be found in future DES data. We have demonstrated the value of deeper imaging to improve the photometric errors and to detect stars at and below the MSTO. This greatly improves the fitting of isochrones, in particular tightening the constraints on the age. For many of these newly discovered objects a wide field is not needed and SOI on the SOAR telescope is an ideal instrument for follow-up studies.

ACKNOWLEDGEMENTS

This paper has gone through internal review by the DES collaboration.

Funding for the DES Projects has been provided by the U.S. Department of Energy, the U.S. National Science Foundation, the Ministry of Science and Education of Spain, the Science and Technology Facilities Council of the United Kingdom, the Higher Education Funding Council for England, the National Center for Supercomputing Applications at the University of Illinois at Urbana-Champaign, the Kavli Institute of Cosmological Physics at the University of Chicago, the Center for Cosmology and Astro-Particle Physics at the Ohio State University, the Mitchell Institute for Fundamental Physics and Astronomy at Texas A&M University, Financiadora de Estudos e Projetos, Fundação

Carlos Chagas Filho de Amparo à Pesquisa do Estado do Rio de Janeiro, Conselho Nacional de Desenvolvimento Científico e Tecnológico and the Ministério da Ciência, Tecnologia e Inovação, the Deutsche Forschungsgemeinschaft and the Collaborating Institutions in the Dark Energy Survey.

The Collaborating Institutions are Argonne National Laboratory, the University of California at Santa Cruz, the University of Cambridge, Centro de Investigaciones Energéticas, Medioambientales y Tecnológicas-Madrid, the University of Chicago, University College London, the DES-Brazil Consortium, the University of Edinburgh, the Eidgenössische Technische Hochschule (ETH) Zürich, Fermi National Accelerator Laboratory, the University of Illinois at Urbana-Champaign, the Institut de Ciències de l'Espai (IEEC/CSIC), the Institut de Física d'Altes Energies, Lawrence Berkeley National Laboratory, the Ludwig-Maximilians Universität München and the associated Excellence Cluster Universe, the University of Michigan, the National Optical Astronomy Observatory, the University of Nottingham, The Ohio State University, the University of Pennsylvania, the University of Portsmouth, SLAC National Accelerator Laboratory, Stanford University, the University of Sussex, Texas A&M University, and the OzDES Membership Consortium.

Based in part on observations at Cerro Tololo Inter-American Observatory, National Optical Astronomy Observatory, which is operated by the Association of Universities for Research in Astronomy (AURA) under a cooperative agreement with the National Science Foundation.

The DES data management system is supported by the National Science Foundation under Grant Numbers AST-1138766 and AST-1536171. The DES participants from Spanish institutions are partially supported by MINECO under grants AYA2015-71825, ESP2015-88861, FPA2015-68048, SEV-2012-0234, SEV-2016-0597, and MDM-2015-0509, some of which include ERDF funds from the European Union. IFAE is partially funded by the CERCA program of the Generalitat de Catalunya. Research leading to these results has received funding from the European Research Council under the European Union's Seventh Framework Program (FP7/2007-2013) including ERC grant agreements 240672, 291329, and 306478. We acknowledge support from the Australian Research Council Centre of Excellence for All-sky Astrophysics (CAASTRO), through project number CE110001020.

This manuscript has been authored by Fermi Research Alliance, LLC under Contract No. DE-AC02-07CH11359 with the U.S. Department of Energy, Office of Science, Office of High Energy Physics. The United States Government retains and the publisher, by accepting the article for publication, acknowledges that the United States Government retains a non-exclusive, paid-up, irrevocable, world-wide license to publish or reproduce the published form of this manuscript, or allow others to do so, for United States Government purposes.

Based on observations obtained at the Southern Astrophysical Research (SOAR) telescope, which is a joint project of the Ministério da Ciência, Tecnologia, e Inovação (MCTI) da República Federativa do Brasil, the U.S. National Optical Astronomy Observatory (NOAO), the University of North Carolina at Chapel Hill (UNC), and Michigan State University (MSU).

REFERENCES

Balbinot E., et al., 2013, ApJ, 767, 101
Balbinot E., et al., 2015, MNRAS, 449, 1129
Bechtol K., et al., 2015, ApJ, 807, 50
Belokurov V., et al., 2010, ApJ, 712, L103
Bertin E., 2011, in Evans I. N., Accomazzi A., Mink D. J., Rots A. H., eds, Astronomical Society of the Pacific Conference Series Vol. 442, Astronomical Data Analysis Software and Systems XX. p. 435
Bertin E., Arnouts S., 1996, A&AS, 117, 393
Bressan A., Marigo P., Girardi L., Salasnich B., Dal Cero C., Rubele S., Nanni A., 2012, MNRAS, 427, 127
Carraro G., Bensby T., 2009, MNRAS, 397, L106
Davis M., Efstathiou G., Frenk C. S., White S. D. M., 1985, ApJ, 292, 371
Desai S., et al., 2012, ApJ, 757, 83
Dooley G. A., Peter A. H. G., Carlin J. L., Frebel A., Bechtol K., Willman B., 2017, preprint, (`arXiv:1703.05321`)
Drlica-Wagner A., et al., 2015, ApJ, 813, 109
Drlica-Wagner A., et al., 2016, ApJ, 833, L5
Drlica-Wagner A., et al., 2017, preprint, (`arXiv:1708.01531`)
Fadely R., Willman B., Geha M., Walsh S., Muñoz R. R., Jerjen H., Vargas L. C., Da Costa G. S., 2011, AJ, 142, 88
Flaugher B., et al., 2015, AJ, 150, 150
Font A. S., et al., 2011, MNRAS, 417, 1260
Foreman-Mackey D., Hogg D. W., Lang D., Goodman J., 2013, PASP, 125, 306
Harris W. E., 2010, preprint, (`arXiv:1012.3224`)
Homma D., et al., 2016, ApJ, 832, 21
Homma D., et al., 2017, preprint, (`arXiv:1704.05977`)
Ibata R. A., Gilmore G., Irwin M. J., 1994, Nature, 370, 194
Ibata R., Nipoti C., Sollima A., Bellazzini M., Chapman S. C., Dalessandro E., 2013, MNRAS, 428, 3648
Jester S., et al., 2005, AJ, 130, 873
Jethwa P., Erkal D., Belokurov V., 2016, MNRAS, 461, 2212
Kim D., Jerjen H., 2015a, ApJ, 799, 73
Kim D., Jerjen H., 2015b, ApJ, 808, L39
Kim D., Jerjen H., Milone A. P., Mackey D., Da Costa G. S., 2015, ApJ, 803, 63
Kim D., Jerjen H., Mackey D., Da Costa G. S., Milone A. P., 2016a, ApJ, 820, 119
Kim D., et al., 2016b, ApJ, 833, 16
Koposov S., et al., 2007, ApJ, 669, 337
Koposov S. E., Belokurov V., Torrealba G., Evans N. W., 2015a, ApJ, 805, 130
Koposov S. E., et al., 2015b, ApJ, 811, 62
Koposov S. E., Belokurov V., Torrealba G., 2017, MNRAS, 470, 2702
Kroupa P., 2001, MNRAS, 322, 231
Laevens B. P. M., et al., 2014, ApJ, 786, L3
Laevens B. P. M., et al., 2015a, ApJ, 802, L18
Laevens B. P. M., et al., 2015b, ApJ, 813, 44
Law D. R., Majewski S. R., 2010, ApJ, 714, 229
Li T. S., et al., 2017, ApJ, 838, 8
Luque E., et al., 2016, MNRAS, 458, 603
Luque E., et al., 2017, MNRAS, 468, 97
Mackey A. D., Gilmore G. F., 2004, MNRAS, 355, 504
Mackey A. D., van den Bergh S., 2005, MNRAS, 360, 631
Marino A. F., Milone A. P., et al. 2014, MNRAS, 442, 3044
Marino A. F., et al., 2015, MNRAS, 450, 815
Martin N. F., de Jong J. T. A., Rix H.-W., 2008, ApJ, 684, 1075
Martin N. F., et al., 2015, ApJ, 804, L5
McConnachie A. W., 2012, AJ, 144, 4
Milone A. P., et al., 2014, ApJ, 785, 21
Mohr J. J., Armstrong R., Bertin E., et al. 2012, in Society of Photo-Optical Instrumentation Engineers (SPIE) Conference Series. p. 0 (`arXiv:1207.3189`), doi:10.1117/12.926785

Muñoz R. R., Geha M., Côté P., Vargas L. C., Santana F. A., Stetson P., Simon J. D., Djorgovski S. G., 2012, ApJ, 753, L15

Nidever D. L., Majewski S. R., Butler Burton W., 2008, ApJ, 679, 432

Odenkirchen M., Grebel E. K., Dehnen W., Rix H.-W., Wolf C., Rockosi C. M., 2002, in Grebel E. K., Brandner W., eds, Astronomical Society of the Pacific Conference Series Vol. 285, Modes of Star Formation and the Origin of Field Populations. p. 184

Pieres A., et al., 2016, MNRAS, 461, 519

Plummer H. C., 1911, MNRAS, 71, 460

Rockosi C. M., et al., 2002, AJ, 124, 349

Sales L. V., Navarro J. F., Kallivayalil N., Frenk C. S., 2017, MNRAS, 465, 1879

Schlegel D. J., Finkbeiner D. P., Davis M., 1998, ApJ, 500, 525

Sevilla I., Armstrong R., et al. 2011, preprint, (`arXiv:1109.6741`)

Simon J. D., et al., 2015, ApJ, 808, 95

Simon J. D., et al., 2017, ApJ, 838, 11

Szabo T., Pierpaoli E., Dong F., Pipino A., Gunn J., 2011, ApJ, 736, 21

The Dark Energy Survey Collaboration 2005, preprint, (`arXiv:astro-ph/0510346`)

Torrealba G., et al., 2016a, MNRAS,

Torrealba G., Koposov S. E., Belokurov V., Irwin M., 2016b, MNRAS, 459, 2370

Walker M. G., Mateo M., Olszewski E. W., Bailey III J. I., Koposov S. E., Belokurov V., Evans N. W., 2015, ApJ, 808, 108

Walker M. G., et al., 2016, ApJ, 819, 53

White S. D. M., Rees M. J., 1978, MNRAS, 183, 341

Willman B., Strader J., 2012, AJ, 144, 76

York D. G., Adelman J., Anderson Jr. J. E., Anderson S. F., et al. 2000, AJ, 120, 1579

Zinn R., 1985, ApJ, 293, 424

Zinn R., 1993, in Smith G. H., Brodie J. P., eds, Astronomical Society of the Pacific Conference Series Vol. 48, The Globular Cluster-Galaxy Connection. p. 38

[1] *Instituto de Física, UFRGS, Caixa Postal 15051, Porto Alegre, RS - 91501-970, Brazil*

[2] *Laboratório Interinstitucional de e-Astronomia - LIneA, Rua Gal. José Cristino 77, Rio de Janeiro, RJ - 20921-400, Brazil*

[3] *George P. and Cynthia Woods Mitchell Institute for Fundamental Physics and Astronomy, and Department of Physics and Astronomy, Texas A&M University, College Station, TX 77843, USA*

[4] *Fermi National Accelerator Laboratory, P. O. Box 500, Batavia, IL 60510, USA*

[5] *Kavli Institute for Cosmological Physics, University of Chicago, Chicago, IL 60637, USA*

[6] *Department of Physics, University of Surrey, Guildford GU2 7XH, UK*

[7] *Observatório Nacional, Rua Gal. José Cristino 77, Rio de Janeiro, RJ 20921-400, Brazil*

[8] *Cerro Tololo Inter-American Observatory, National Optical Astronomy Observatory, Casilla 603, La Serena, Chile*

[9] *Department of Physics & Astronomy, University College London, Gower Street, London, WC1E 6BT, UK*

[10] *Department of Physics and Electronics, Rhodes University, PO Box 94, Grahamstown, 6140, South Africa*

[11] *LSST, 933 North Cherry Avenue, Tucson, AZ 85721, USA*

[12] *CNRS, UMR 7095, Institut d'Astrophysique de Paris, F-75014, Paris, France*

[13] *Sorbonne Universités, UPMC Univ Paris 06, UMR 7095, Institut d'Astrophysique de Paris, F-75014, Paris, France*

[14] *Department of Astronomy, University of Illinois, 1002 W. Green Street, Urbana, IL 61801, USA*

[15] *National Center for Supercomputing Applications, 1205 West Clark St., Urbana, IL 61801, USA*

[16] *Institut de Física d'Altes Energies (IFAE), The Barcelona Institute of Science and Technology, Campus UAB, 08193 Bellaterra (Barcelona) Spain*

[17] *Institute of Space Sciences, IEEC-CSIC, Campus UAB, Carrer de Can Magrans, s/n, 08193 Barcelona, Spain*

[18] *Kavli Institute for Particle Astrophysics & Cosmology, P. O. Box 2450, Stanford University, Stanford, CA 94305, USA*

[19] *Department of Physics, California Institute of Technology, Pasadena, CA 91125, USA*

[20] *Jet Propulsion Laboratory, California Institute of Technology, 4800 Oak Grove Dr., Pasadena, CA 91109, USA*

[21] *Instituto de Fisica Teorica UAM/CSIC, Universidad Autonoma de Madrid, 28049 Madrid, Spain*

[22] *Department of Astronomy, University of Michigan, Ann Arbor, MI 48109, USA*

[23] *Department of Physics, University of Michigan, Ann Arbor, MI 48109, USA*

[24] *SLAC National Accelerator Laboratory, Menlo Park, CA 94025, USA*

[25] *Center for Cosmology and Astro-Particle Physics, The Ohio State University, Columbus, OH 43210, USA*

[26] *Department of Physics, The Ohio State University, Columbus, OH 43210, USA*

[27] *Astronomy Department, University of Washington, Box 351580, Seattle, WA 98195, USA*

[28] *Australian Astronomical Observatory, North Ryde, NSW 2113, Australia*

[29] *Institució Catalana de Recerca i Estudis Avançats, E-08010 Barcelona, Spain*

[30] *Institute of Cosmology & Gravitation, University of Portsmouth, Portsmouth, PO1 3FX, UK*

[31] *Centro de Investigaciones Energéticas, Medioambientales y Tecnológicas (CIEMAT), Madrid, Spain*

[32] *School of Physics and Astronomy, University of Southampton, Southampton, SO17 1BJ, UK*

[33] *Instituto de Física Gleb Wataghin, Universidade Estadual de Campinas, 13083-859, Campinas, SP, Brazil*

[34] *Computer Science and Mathematics Division, Oak Ridge National Laboratory, Oak Ridge, TN 37831*

This paper has been typeset from a TEX/LATEX file prepared by the author.